Available online at www.sciencedirect.com
ScienceDirect
Cement and Concrete Research 37 (2007) 502–511
Cement and Concrete Research

Non-ideal solid solution aqueous solution modeling of synthetic calcium silicate hydrate

Colin S. Walker [a,*], David Savage [b], Mark Tyrer [c], K. Vala Ragnarsdottir [a]

[a] Department of Earth Sciences, University of Bristol, Wills Memorial Building, Queen's Road, Bristol, BS8 1RJ, UK
[b] Quintessa Limited, Dalton House, Newtown Road, Henley-on-Thames, RG9 1HG, UK
[c] Department of Materials, Imperial College, South Kensington, London, SW7 2AZ, UK

Received 9 February 2006; accepted 5 December 2006

Abstract

New data relevant to calcium silicate hydrate (C–S–H) gels prepared at room temperature have been obtained over a time period of up to 112 weeks. X-ray diffraction (XRD) indicates equilibrium was attained after 64 weeks. Coupled with fourier transform infrared (FT-IR) spectroscopy, a phase change in C–S–H gel at Ca/Si ≈ 1.0 was identified and the occurrence of portlandite as a distinct phase for Ca/Si > 1.64. The incongruent dissolution of C–S–H gel was modeled as a non-ideal solid solution aqueous solution (SSAS) between the end-member components CaH_2SiO_4 (CSH) and $Ca(OH)_2$ (CH) using equations defining the solidus and solutus curves on a Lippmann phase diagram. Despite being semi-empirical, the model provides a reasonable and consistent fit to the solubility data and can therefore be used to describe the incongruent dissolution of C–S–H gels with compositions Ca/Si ≥ 1.0.

Keywords: A. pH; B. calcium silicate hydrate (C–S–H); C. $Ca(OH)_2$; E. Modeling

1. Introduction

It is generally agreed that the safe disposal of low and intermediate level radioactive wastes should be in purpose built repositories buried deep in the geosphere [1–3]. Favored repository designs anticipate the extensive use of Ordinary Portland Cement (OPC) based materials [3–6]. OPC was chosen because of its widespread use in construction and its ability to provide a high pH buffer for invading groundwaters. A high pH in the repository is desirable because it helps to minimize the solubility of many radionuclides, metal corrosion and microbial activity [6–9]. In the long-term (ideally in excess of 10^5 years) the most important phase believed to control the pH is C–S–H gel [3,7]; the non-stoichiometric acronym C–S–H is derived from cement chemistry shorthand: C—CaO, S—SiO_2 and H—H_2O.

Despite forming 40–60% of OPC [3,10], the true structure of C–S–H gel has yet to be resolved because it is near amorphous and has a variable composition on the nanometer scale [11–14]. For simplicity C–S–H gel is often referred to by its bulk composition in terms of Ca/Si ratio, which in OPC varies from 1.5 to 2.0 [15]. In a repository this bracket value is expected to decline with time because C–S–H gel dissolves incongruently with the release of aqueous calcium being much higher than that of silicon, especially for Ca/Si > 1.0. As the Ca/Si ratio of C–S–H gel declines, so too will its ability to buffer the pH of invading groundwaters [9]. This solubility behaviour has been observed in numerous experimental studies using synthetically prepared C–S–H gels [16–24]. Using synthetic C–S–H gels ensures a satisfactory level of purity and allows the pH, and calcium and silicon concentrations to be cited as a function of Ca/Si ratio of the solid phase(s), including contributions from amorphous silica ($S_{(am)}$) and CH. These studies however, lack consistency because of the difference in synthetic methods employed,

* Corresponding author. Present address: Department of Mineralogy, The Natural History Museum, Cromwell Road, London, SW7 5BD, UK. Tel.: +44 774 757 9736; fax: +44 20 7942 5537.
E-mail address: c.walker@nhm.ac.uk (C.S. Walker).

0008-8846/$ - see front matter © 2006 Elsevier Ltd. All rights reserved.
doi:10.1016/j.cemconres.2006.12.002

Table 1
Experimental conditions used to derive previous C–S–H solubility data

Method	T (°C)	Duration	Water/solid ratio [a]	Carbonate (wt.%)	References
Direct reaction (DR)	30	1 month	NR	NR	[16]
Double decomposition (DD)	30.2	≤8 days	<800	0.07	[17]
C_3S hydrationi, DR[ii] & DD[iii]	17–20	≤80 days	[i]90–475 [ii]102 [iii]NR	0.66–4.8	[18]
DR	25	≤100 days	529–1701	NR	[19]
DR	50(50) then 25(34)	84 days	45–102	NR	[20]
DD	30	1–6 months	471–2500	<2.5	[21]
DD [b]	25	65 weeks	8 [c]	NR	[22]
DR [b]	25(2) then 40(4)	6 months	100	NR	[23]
C_3S hydration and DD	22	2–6 weeks	50–4000	NR	[24]
DR	20–25	1–112 weeks	10	0.03–0.2	This study

Notes:
DR — mixing solutions of CH and SiO_2.
DD — mixing solutions containing sodium silicate and a soluble calcium salt.
C_3S — tricalcium silicate (Ca_3SiO_5).
NR — not reported.
Parentheses under the T (°C) column indicate time at this temperature, units given under the Duration column.
Only those experiments undertaken at near room temperature and reporting the final Ca/Si ratio of the solid phases(s), either measured or calculated are shown. Also shown are the experimental conditions used in this study.
[a] Water/solid ratio (by mass) for C_3S includes water added for leaching to reduce the Ca/Si ratio in the solid phase(s) and for DD accounts for solution concentrations.
[b] Atkinson et al [22] and Cong and Kirkpatrick [23] also conducted DR and C_2S hydration experiments, respectively, but these are not considered in this paper.
[c] Solids were filtered then re-dispersed in pure water.

reaction temperatures, equilibration times, water/solid ratios, and largely unknown degrees of carbonation (Table 1).

There is a wide distribution in the so derived solubility data for C–S–H gel, especially for calcium and silicon concentrations for Ca/Si>1.0 (Fig. 1). Part of the scatter could be explained by the water/solid ratio used and whether the reported Ca/Si ratio represents the entire system, including dissolved calcium and silicon, or the solid phase(s) alone. To minimize this effect, only those solubility data are shown for which the final Ca/Si ratio of the solid phase(s) has been either measured [17–19,21–24] or calculated [16,20]. The experimental conditions are overall too varied to justify this distribution, with the possible exception of Greenberg and Chang [20] whose use of higher temperatures appear to have suppressed the solubility of C–S–H gel because of a possible increase in crystallinity [3]. Despite these variations, the solubility data provided by these studies are frequently taken at face value as being representative of the dissolution behaviour of C–S–H gel.

Because of the long time frames necessary for the isolation of radioactive wastes, the incongruent dissolution of C–S–H gel requires deterministic modeling, which must account for the experimentally observed changes in pH, and calcium and silicon concentrations as a function of Ca/Si ratio in the solid phase(s). The conventional modeling approach is to take either one or two pure solid phases with variable solubility products and adjust the model parameters until a match is made with the data [25,26]. A thermodynamically defensible approach, however, describes the incongruent dissolution of C–S–H gel as a solid solution aqueous solution (SSAS). This approach can be solved in two ways, either using two independent ideal SSAS based on Gibbs energy minimization (GEM) algorithms [27–29] or a single non-ideal SSAS based on law of mass-action equations [30–32].

The two independent ideal SSAS model used end-member components of (i) $S_{(am)}$–$(CH)_5S_6H_5$ and (ii) $(CH)_5S_6H_5$–$(CH)_{10}S_6H_5$, where $(CH)_5S_6H_5$ was chosen to approximate tobermorite-like C–S–H(I) and $(CH)_{10}S_6H_5$ to approximate jennite-like C–S–H(II) [33], with CH present for higher Ca/Si ratios. This model can therefore describe the solubility behaviour of C–S–H gels for all Ca/Si ratios. Both ideal SSAS were solved using GEM algorithms, embodied in the computer program Selektor-A [34] (superceded by GEMS [35]) to provide the best model fit to the solubility data of Greenberg and Chang [20]. Despite being a more elaborate SSAS model, this approach is not readily transparent at present and is undergoing further development by the authors. Consequently, this paper will describe the incongruent dissolution of C–S–H gel using the single non-ideal SSAS modeling approach.

The single non-ideal SSAS models [30–32] used end-member components of C–S–H gel (Ca/Si=1.0 in all cases) and CH, thereby accounting for the solubility behavior of the solid phase(s) with Ca/Si≥1.0, where incongruent dissolution is most marked (Fig. 1). This modeling approach also included a miscibility gap, where the two end-members coexist over a given range of Ca/Si compositions, typically expressed as a mole fraction of CH, X_{CH}, where:

$$X_{CH} = 1 - \frac{1}{Ca/Si}. \quad (1)$$

Even with the rigors of this approach, there still remains some doubt over the choice of solubility data used to derive the solubility product, K_{sp}, of the C–S–H gel end-member, the

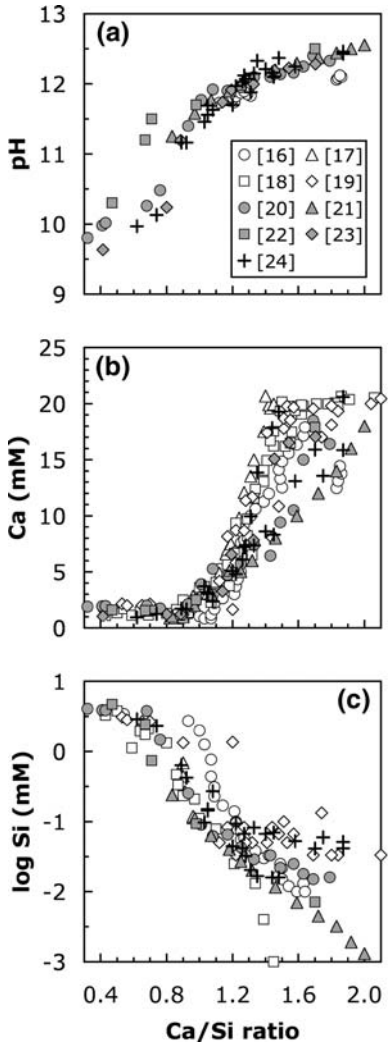

Fig. 1. Solubility data compilation for synthetic C–S–H gels prepared near room temperature shown as a function of Ca/Si ratio of the solid phase(s). The Ca/Si ratios were either measured [17–19,21–24] or calculated [16,20] after their respective experiment duration (Table 1) and include contributions from $S_{(am)}$ and CH. Figure legend: [16] Flint and Wells, 1934; [17] Roller and Ervin, 1940; [18] Taylor, 1950; [19] Kalousek, 1952; [20] Greenberg and Chang, 1965; [21] Fujii and Kondo, 1981; [22] Atkinson et al., 1987; [23] Cong and Kirkpatrick, 1996; [24] Chen et al., 2004. (a) pH: (b) Ca (mM): (c) log Si (mM).

miscibility gaps they used and the inconsistency in using data from several sources (Table 2).

Given the uncertainties in the C–S–H solubility data and the non-ideal SSAS models on which these were based, we considered that it was necessary to derive new solubility and miscibility gap data and redefine a non-ideal SSAS model based on these data alone.

2. Non-ideal SSAS model

The non-ideal SSAS model presented in this paper adopts the theoretical basis of SSAS developed by Lippmann [40–42] and Glynn and co-workers [43–45], as did Kersten [30], thereby reiterating a majority of Kersten's modeling work.

The end-member components chosen to represent the SSAS were CSH (Ca/Si = 1.0) and CH, previously used by Börjesson et al. [31] and Rahman et al. [32]. CSH is an empirical formula representing the simplest stoichiometry of a C–S–H gel expressed by its component oxides.

The dissolution reactions of the end-member components, CSH and CH, are expressed in terms of Ca^{2+}, $HSiO_3^-$ and OH^-. Ca^{2+} and OH^- are therefore common to both end-members and the SSAS is governed by the substitution of OH^- for $HSiO_3^-$ with increasing Ca/Si ratio.

Assuming a C–S–H gel synthesized at room temperature can achieve true thermodynamic equilibrium, the dissolution of the CSH–CH SSAS can be described by the total solubility product, $\sum \Pi_{sp}$ [41,42]:

$$\sum \Pi_{sp} = K_{CSH} X_{CSH} \gamma_{CSH} + K_{CH} X_{CH} \gamma_{CH} \quad (2)$$

where K_{CSH} and K_{CH} are the K_{sp} values of the pure end-members CSH and CH; X_{CSH} and X_{CH} are the mole fractions of CSH and CH in the equilibrium solid; and γ_{CSH} and γ_{CH} represent the solid phase activity coefficients of CSH and CH. Eq. (2) defines the solidus on a Lippmann phase diagram [41,42], where the log value of $\sum \Pi_{sp}$ can be plotted on the ordinate against X_{CH} on the bottom abscissa.

The K_{sp} values of the pure end-members CSH ($X_{CSH} = \gamma_{CSH} = 1$) and CH ($X_{CH} = \gamma_{CH} = 1$) can be calculated according to:

$$K_{CSH} = \{Ca^{2+}\}\{HSiO_3^-\}\{OH^-\} \quad (3)$$

$$K_{CH} = \{Ca^{2+}\}\{OH^-\}^2 \quad (4)$$

where {} denote activities in solution. Using geochemical computer programs, such as PHREEQC [46], the activities of these species in solution can be calculated from experimental solubility data. The solid phase activity coefficients, γ_{CSH} and γ_{CH}, are calculated from Guggenheim parameters, α_0 and α_1, which are used to describe the excess Gibbs free energy of mixing of a non-ideal subregular binary solid solution expressed as a function of X_{CSH} and X_{CH} [47–49]. The values of α_0 and α_1 can be solved using either computer program PHREEQC or MBSSAS [39] from the lower and upper miscibility gap compositional boundaries. The lower miscibility gap compositional boundary, $X_{CH,1}$, can be determined analytically using XRD and FT-IR spectroscopy by the occurrence of CH. The upper miscibility gap compositional boundary, $X_{CH,2}$, should perhaps be set to 1.0, however, using $X_{CH,2} = 1.0$ returns a null result for the values of α_0 and α_1. Instead, the model becomes semi-empirical because $X_{CH,2}$ is determined by fitting the solidus to the solubility data in the CSH–CH SSAS using a least squares fitting algorithm.

To fully describe the SSAS at equilibrium, $\sum \Pi_{sp}$ can also be related to the composition of the solution [43]:

$$\sum \Pi_{sp} = \frac{1}{\frac{\chi_{HSiO_3^-}}{K_{CSH}\gamma_{CSH}} + \frac{\chi_{OH^-}}{K_{CH}\gamma_{CH}}} \quad (5)$$

where $\chi_{HSiO_3^-}$ and χ_{OH^-} are aqueous activity fractions of $HSiO_3^-$ and OH^-, respectively. Eq. (5) defines the solutus on a Lippmann phase diagram, where the log value of $\sum \Pi_{sp}$ can

Table 2
Dissolution reactions, solubility products and miscibility gaps used in previous non-ideal CSH–CH SSAS models

References	Dissolution reactions	Log K_{sp}	Data source	Miscibility gap		Data source
				Ca/Si	Mole fraction ($X_{CH,1}$, $X_{CH,2}$)	
[30]	$0.5(Ca_2H_2Si_2O_7{\cdot}3H_2O) \rightleftharpoons Ca^{2+}+H_2SiO_4^{2-}+H_2O$	−8.07	[16–18,20,21]	>3	0.67, 0.95	[a]
	$Ca(OH)_2 \rightleftharpoons Ca^{2+}+2OH^-$	−5.22	NR			
[31]	$CaH_2SiO_4 \rightleftharpoons Ca^{2+}+H_2SiO_4^{2-}$	−7.07	[20]	>1.43	0.3, 0.99	Fitted to [19]
	$Ca(OH)_2 \rightleftharpoons Ca^{2+}+2OH^-$	−5.19	[36]			
[32]	$CaH_2SiO_4 \rightleftharpoons Ca^{2+}+H_2SiO_4^{2-}$	−8.16	[16–21]	>1.5	0.33, 0.99	[15,37,38]
	$Ca(OH)_2 \rightleftharpoons Ca^{2+}+2OH^-$	−5.15				

Notes:
Dissolution reactions of CSH and CH have been written in this convention for direct comparison.
NR — not reported.
[a] The lower miscibility gap, $X_{CH,1}=0.67$ from C_3S hydration, despite CH being a reaction product, and the upper miscibility gap, $X_{CH,2}=0.95$ from the limitation of using MBSSAS [39].

be plotted on the ordinate against χ_{OH^-} on the bottom abscissa, which is superimposed on X_{CH} associated with the solidus curve.

Consequently, using Eqs. (2) and (5) it was possible to construct a Lippmann phase diagram, which could be used to describe the solubility of C–S–H gel as a function of its composition for Ca/Si ≥ 1.0. Furthermore, the same theoretical basis of non-ideal SSAS modeling has been added to PHREEQC [49], whereby encoding the K_{sp} values of the end-member components and miscibility gap compositional boundaries provided a quantitative prediction of pH, and calcium and silicon concentrations as a function of Ca/Si ratio.

3. Experimental

3.1. Preparation of CSH, C–S–H gel and solubility experiments

Both CSH and C–S–H gels were synthesized using the direct reaction method where CaO and SiO_2 powders were mixed in water to a specific Ca/Si ratio. Ensuring these reagents were pure required some preliminary treatment. CaO was heated at 1100 °C for 6 hours and transferred to the airlock of a glove box while incandescent. SiO_2 was bought as silica fume and acid washed (1 M HCl and 1 M HNO_3), further cleansed by dialysis for 4 months and oven dried at 120 °C for a week. Deionized water (18.2 MΩ cm) was boiled and subsequently cooled under a low CO_2 atmosphere using high purity nitrogen with <1 ppm CO_2.

All treated reagents were mixed in a glove box under a low CO_2 atmosphere (<1 ppm) at 20–25 °C and 60–70% relative humidity. CaO and silica fume were weighed to give a specific Ca/Si ratio with a combined total mass of 3 g. Chosen Ca/Si ratios were 0.4, 0.6, 0.8, 0.9, 1.0 (CSH), 1.1, 1.2, 1.4, 1.6, 1.7, 1.8, and 2.0. The 3 g mixture was added to a 50 ml HDPE centrifuge tube containing 30 ml of deionized water and sealed, giving a water/solid ratio = 10. After loading the centrifuge tubes, they were removed from the glove box and agitated continuously throughout their respective experimental run times. Chosen experimental run times were 1, 2, 4, 8, 16, 32, 48, 64, 80, 96, and 112 weeks and temperature was maintained between 20 and 25 °C. When the reaction time was complete, the samples were centrifuged at 12,000 rpm for 10 min to separate the solid from the liquid phase. The centrifuge tubes were returned to the glove box and the liquids decanted into separate tubes. All tubes were resealed leaving the separated solid and liquid phases ready for analysis.

It should be noted that several of the reported run products for any given week were not always all prepared at the same time. Hence, the consistency of the data, or lack thereof, cannot be related to loading conditions on any given day.

3.2. Characterization of solids and solutions

The Ca/Si ratio of the solid phase(s) was determined after their respective experimental run times using a standard lithium metaborate ($LiBO_2$) fusion method [50]. Solid phases were further characterized using powder position sensitive detector XRD (PSD-XRD) and FT-IR spectroscopy to verify the presence of a unique solid at Ca/Si = 1.0, confirming the validity of CSH as an end-member, and the occurrence of CH as a distinct phase, thereby providing the value of $X_{CH,1}$. Carbonate contents were determined using a modified version of the Conway diffusion method [51] to assess the purity of the synthesized solid phases and hence the validity of the solubility data.

Before decomposing in $LiBO_2$, the solids were weighed before and after overnight drying at 120 °C to determine the amount of excess water remaining in the solid phase(s) after centrifugation. The measured Ca/Si ratio of the solid phase(s) could therefore be corrected knowing the calcium and silicon concentrations of the excess water.

PSD-XRD patterns of wet samples were collected with an INEL CPS-120 curved position-sensitive detector [52,53] with around 3200 points over 1–120° in 2θ giving an interval of about 0.037° 2θ. A 1500 W copper sealed tube (25 mA at 40 kV) and Ge 111 monochromator provided monochromatic CuKα1 ($\lambda = 1.5406$ Å) radiation. Collection times were usually 1000 min, or more, giving the most intense basal reflection a height of 1.5×10^5 counts and the weakest basal reflection (where identifiable) a height of 1.0×10^4 counts, the background intensity was approximately 2.5×10^3 on average.

FT-IR spectra of wet samples were acquired in the mid-region (400–5000 cm^{-1}) using a Nicolet 800 FTIR Spectrometer. A

Table 3
Aqueous reactions and their respective equilibrium constants at 25 °C

Reaction	Log K_{eq}
$OH^- + H^+ \rightleftharpoons H_2O$	13.9951
$CaOH^+ + H^+ \rightleftharpoons Ca^{2+} + H_2O$	12.85
$SiO_2 + H_2O \rightleftharpoons HSiO_3^- + H^+$	−9.9525
$SiO_2 + 2H_2O \rightleftharpoons H_2SiO_4^{2-} + 2H^+$	−22.96

Taken from the Lawrence Livermore National Laboratory (LLNL) database revision 1.11. This database does not contain any aqueous calcium silicate species.

Globar ceramic beam source, a KBr beam splitter and DTGS detector were used at a resolution of ±4 cm^{-1} with accumulation of 256 scans. Samples were pressed into KBr pellets at a ratio of 1 mg of sample to 100 mg KBr.

Carbonate contents of the solids were determined in triplicate using a modified version of the Conway diffusion method [51]. A known weight of wet sample (≈30 mg) was placed inside a small test tube (25 mm length), which was placed in a 5 ml bottle containing 1 ml of 0.05 M $Ba(OH)_2$ solution. The bottle was sealed with an injectable silicone rubber septum and $HClO_4$ solution (30 wt.%) was injected into the test tube to dissolve the sample and release any carbonate component as CO_2. The apparatus was left overnight to allow the complete dissolution of the sample and all CO_2 to evolve and react to form $BaCO_3$. The quantity of carbonate in the sample was deduced by titrating the remaining $Ba(OH)_2$ with 0.01 M HNO_3.

The liquid phases were characterized by measuring the pH, and calcium and silicon concentrations to provide the necessary solubility data.

The pH values of the solutions were measured with a combined glass electrode calibrated with standard buffer solutions of pH=6, 9.2, 10, and 13. Calibration and measurements were made at room temperature under a low CO_2 atmosphere. The accuracy of the pH measurements was expected to be better than ±0.1 under these conditions.

Calcium and silicon concentrations were determined via ICP-AES using a Jobin Yvon Sequential Spectrometer JY24. Solutions were filtered through 0.2 μm ashless cellulose acetate filters and diluted 1:100 in 1% v/v nitric acid prior to analysis. Calcium was calibrated using standard solutions containing 0, 5, 10, 20, 25 and 50 mg l^{-1} calcium and silicon was calibrated using standard solutions containing 0, 1, 2, 4, 5 and 10 mg l^{-1} silicon. Detection limits for calcium and silicon were 0.03 and 1.5 μg l^{-1}, respectively, and analytical errors were expected to vary from 2% for calcium to 5% for silicon at the concentrations measured.

3.3. Computer codes

The computer program PHREEQC v2.12 [46] was used to calculate the activities of Ca^{2+}, $HSiO_3^-$ and OH^- in solution from the experimentally derived pH, and calcium and silicon concentrations; PHREEQC uses the Davies equation [54] to

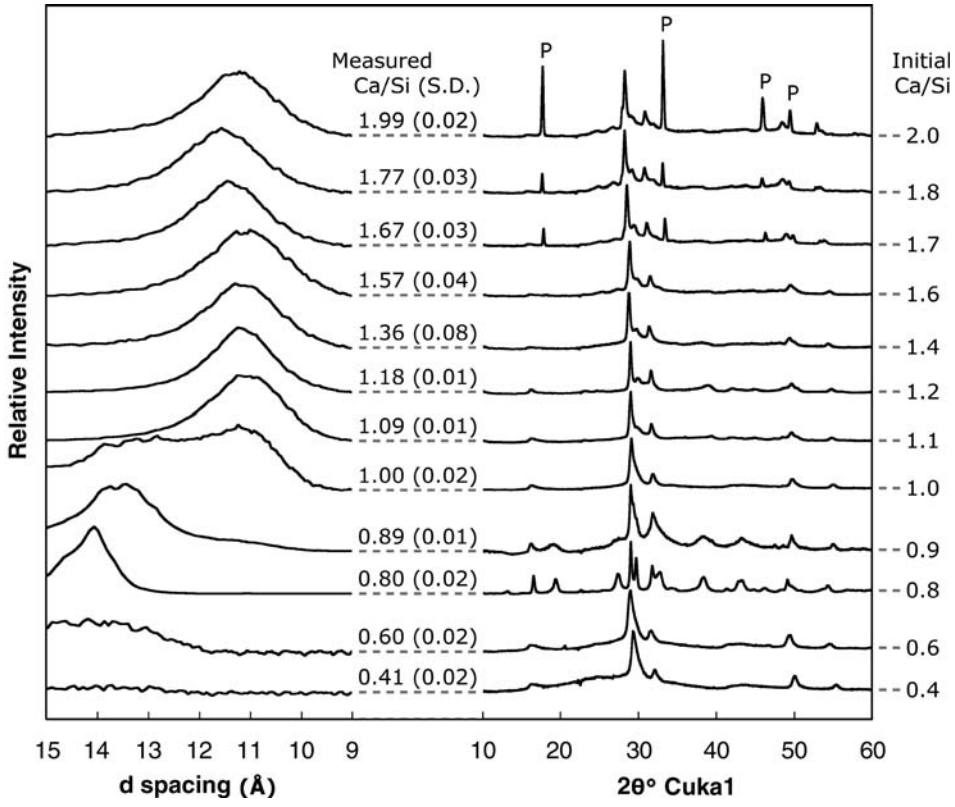

Fig. 2. Powder PSD-XRD scans of representative samples equilibrated for more than 64 weeks. Measured Ca/Si ratios are the mean of samples from weeks 64–112 with standard deviations shown in parentheses. Initial Ca/Si are also indicated on the right hand side for reference. Powder PSD-XRD scans showed a change in basal reflection from 14 Å for Ca/Si=0.80 (identified as 14 Å tobermorite) to 11.2 Å for Ca/Si≥1.09 with Ca/Si=1.00 a mixture of these two C–S–H phases. Peaks assigned to CH are marked with the letter P.

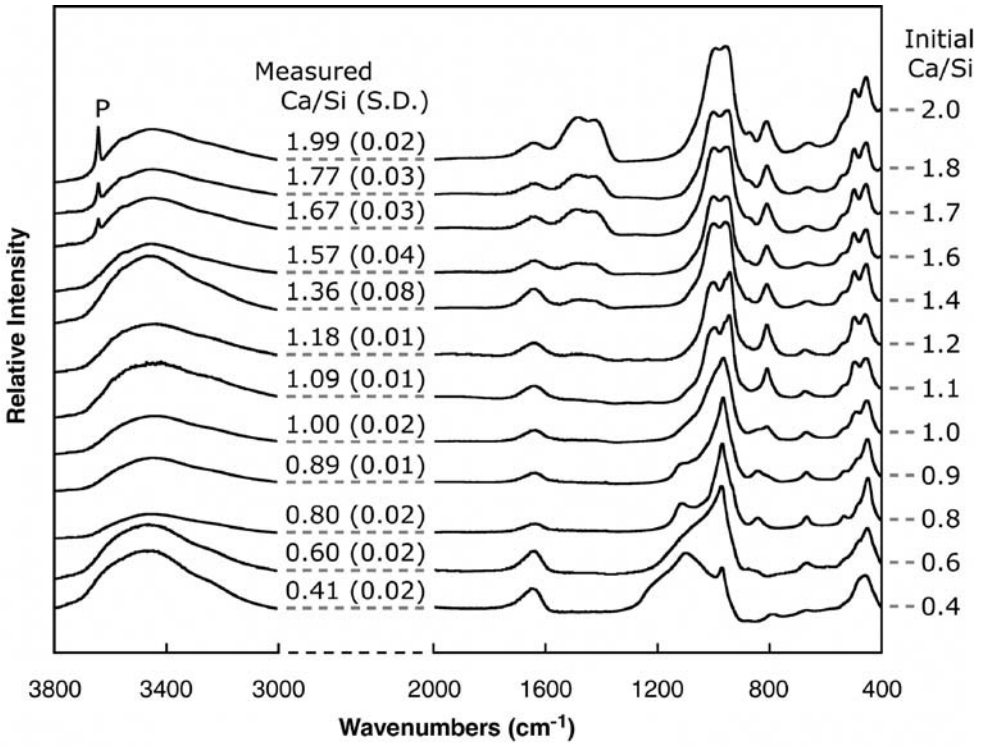

Fig. 3. Mid-region FT-IR spectra showing the absorbance of representative samples equilibrated for more than 64 weeks. Peaks in the FT-IR spectra at 1100 cm^{-1} and 1040 cm^{-1} both disappear for Ca/Si ≥ 1.00, while distinguishable peaks emerge at 808, 940 and 1000 cm^{-1} for Ca/Si = 1.00 with the former becoming sharp and distinct and the latter two becoming two peak maxima with increasing Ca/Si ratio. The sharp peak at 3644 cm^{-1} marked with the letter P was assigned to O–H stretching in CH.

calculate the relevant activity coefficients. This allowed the calculation of K_{CSH} for Ca/Si = 1.0, K_{CH} for all Ca/Si ratios where the more soluble CH was identified by PSD-XRD and FT-IR, $\chi_{HSiO_3^-}$ and χ_{OH^-}. PHREEQC was also used to determine the values of the Guggenheim parameters, α_0 and α_1, based on the experimentally determined lower miscibility gap compositional boundary and fitting the solidus to the solubility data using a least squares fitting algorithm to determine the upper miscibility gap compositional boundary. This allowed the calculation of Eqs. (2) and (5) and the construction of a Lippmann phase diagram. Consequently and perhaps most importantly, with the addition of SSAS modeling capability, PHREEQC could also be used to predict the pH, and calcium and silicon concentrations as a function of Ca/Si ratio of the solid phase(s).

Thermodynamic data for the relevant aqueous species were taken from the Lawrence Livermore National Laboratory (LLNL) database revision 1.11, which comes with PHREEQC (Table 3).

4. Results and discussion

4.1. Characterization of solids and solutions

Overnight drying at 120 °C revealed that approximately 75 wt.% of the centrifuged samples was excess water. Despite this high percentage, the contribution from dissolved calcium and silicon was negligible, only affecting the measured Ca/Si ratio of the solid phase(s) to the third decimal place.

Powder PSD-XRD scans showed the development of a basal reflection after 64 weeks (Fig. 2). This was interpreted as signifying the structural maturity of these synthetic C–S–H gels and equilibrium being reached after this time.

Both powder PSD-XRD scans and FT-IR spectra (Fig. 3) verified a change in the structure of C–S–H gel over the compositional range Ca/Si = 0.80–1.09 and Ca/Si = 1.00–1.09, respectively. These observations support using CSH to represent the C–S–H gel end-member and reaffirms similar findings in previous studies [38,55].

The use and composition of CSH can be justified using the following assumptions. Despite clearly being a mixture (Fig. 2), the 11.2 Å C–S–H phase was the only phase at Ca/Si = 1.00. The 11.2 Å C–S–H phase is more likely related to a tobermorite based structure, which have basal reflections in the range 9.6–14.6 Å [56], as opposed to a jennite based structure, which would have a maximum basal reflection of 10.6 Å [57–60]. Consequently, the 11.2 Å C–S–H phase may well be structurally related to 14 Å tobermorite, which was identified at Ca/Si = 0.80 and has the chemical formula $Ca_5Si_6O_{16}(OH)_2 \cdot 7H_2O$ [61]. The difference between these two phases is probably associated with the loss of silicate tetrahedra with increasing Ca/Si ratio, confirmed by recent ^{29}Si NMR studies [23,24,62,63] and shown to occur at Ca/Si = 1.0 [38,55]. In this case, if the silicate from 14 Å tobermorite was lost as silica, SiO_2, to

maintain charge balance, accompanied by three water molecules from the interlayer position, to account for the observed change in basal reflection (Fig. 2 and [55]), would give a chemical formula $Ca_5Si_5O_{14}(OH)_2{\cdot}4H_2O$ for the 11.2 Å C–S–H phase at Ca/Si = 1.00. Both Taylor's [64] and Richardson and Groves' [65] C–S–H structural models would predict an equivalent chemical formula, $Ca_4Si_5O_{16}H_2Ca{\cdot}4H_2O$ and $Ca_5Si_5H_6O_{17}(OH)_2{\cdot}H_2O$, respectively, assuming there were initially four water molecules in the interlayer position. The chemical formula for the 11.2 Å C–S–H phase can therefore be written simply as $Ca_5H_{10}Si_5O_{20}$, which matches the chosen empirical end-member, CSH.

Both PSD-XRD and FT-IR confirm the presence of CH being a distinct phase for Ca/Si ≥ 1.67 (Figs. 2 and 3). The absolute value for the lower miscibility gap composition was chosen as the mid-point between 1.57 and 1.67, corresponding to $X_{CH,1} = 0.38$.

In keeping with C–S–H gel being represented by a SSAS model for Ca/Si ≥ 1.0, both PSD-XRD and FT-IR show that there were no significant structural changes with increasing Ca/Si ratio, except in the presence of CH where the basal reflection of C–S–H shifts to 11.4 Å (Fig. 2). Reasons for this shift were unclear, either related to the coexistence of CH or to the only other notable difference, the significant carbonate doublet between 1300 and 1600 cm^{-1} in the FT-IR spectra (Fig. 3). However, this was confounded by the absence of any significant increase in the carbonate contents determined by titration, which for Ca/Si ≥ 1.0 had a mean value of 0.12 wt.%, S.D. = 0.04. This low level of carbonation, however, does provide confidence in the validity of the solubility data.

The pH, and calcium and silicon concentrations given as a function of measured Ca/Si ratio show similar trends to those previously derived in other studies [16–24] (Fig. 4), with the exception that pH and calcium concentrations were markedly higher for 0.80 ≤ Ca/Si ≤ 1.57, demonstrating that synthetic C–S–H gels are more soluble than previously thought over this compositional range. Observation of the samples with field emission scanning electron microscopy (not shown) revealed that crystals were either tabular or bladed, depending on Ca/Si ratio, with a common long axis of 100–500 nm. Although possible that some of the smaller crystals may have passed through the 0.2 μm filter used prior to ICP-AES, it seems unlikely because the crystals aggregated to form particles 5–30 μm in diameter, the silicon concentration would also have increased and all Ca/Si ratios should have been affected not just a certain compositional range. Furthermore, the pH and calcium concentrations being similar to those reported by other workers outside the compositional range 0.80 ≤ Ca/Si ≤ 1.57, negates the possibility that the observed increases were an artifact of analytical error. Instead, the increase in pH and calcium concentration may be partly explained by a combination of the relatively low temperature used (20–25 °C) and the low level of carbonate present in the samples. In the context of a nuclear waste repository, this means that C–S–H gel could therefore provide a better pH buffer, but its potential lifespan would be diminished.

With the exception of pH, the reported calcium and silicon concentrations were somewhat diverse in the same compositional range, 0.80 ≤ Ca/Si ≤ 1.57. There were no significant trends related to the maturing of the C–S–H gels over this time frame in terms of the solubility data or their structure shown by PSD-XRD and FT-IR. Thus, the diversity in the solubility data was attributed to varying degrees of carbonation, temperature, crystallinity, and, especially for silicon, analytical error. This illustrates the difficulty in being able to produce consistent solubility data for C–S–H gels, even though the experiments were conducted meticulously under identical conditions.

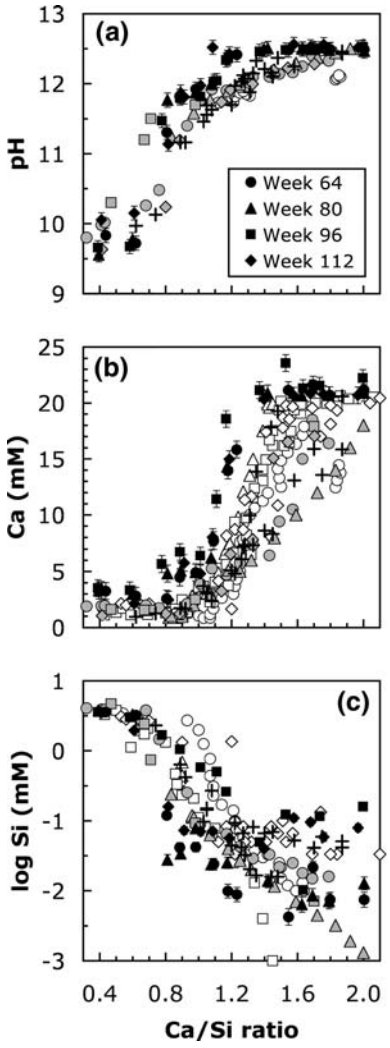

Fig. 4. Solubility data from this study compared to data previously shown in Fig. 1 (same symbols). (a) pH, error ± 0.1: (b) Ca (mM), error ± 2%: (c) log Si (mM), error ± 5%.

4.2. Non-ideal SSAS modeling

The solubility data reported for week 96 were unlike those reported for the other experimental run times (Fig. 4), particularly for Ca/Si = 1.00, used to derive the value of K_{CSH}, and Ca/Si = 1.67–1.99, to derive K_{CH}. Consequently, the C–S–H solubility data from week 96 were omitted from the CSH–CH SSAS modeling. This omission affected the lower miscibility gap composition used in the model, which became the mid-point between 1.58 and 1.69, corresponding to $X_{CH,1} = 0.39$.

Table 4
Summary of thermodynamic data obtained from this study

Dissolution reactions	Log K_{sp}	Miscibility gap		Guggenheim parameters (α_0, α_1)
		Ca/Si	Mole fraction ($X_{CH,1}$, $X_{CH,2}$)	
$CaH_2SiO_4 \rightleftharpoons Ca^{2+}+HSiO_3^-+OH^-$	−8.95	>1.64	0.39, 0.92	1.87, 0.91
$Ca(OH)_2 \rightleftharpoons Ca^{2+}+2OH^-$	−5.13			

Using the computer program PHREEQC to determine the activities of Ca^{2+}, $HSiO_3^-$ and OH^-, the K_{sp} values of the pure end-members CSH and CH were calculated according to Eqs. (3) and (4) to be log $K_{CSH}=-8.95$, S.D.=0.14, and log $K_{CH}=-5.13$, S.D.=0.04 (Table 4).

Expressing the dissolution reaction of CSH in terms of Ca^{2+} and $H_2SiO_4^{2-}$ would give log $K_{CSH}=-7.96$, which is in good agreement with the log K_{CSH} values used by Kersten [30] and Rahman et al. [32] (Table 2). This is perhaps not surprising considering the similarity of the solubility data at Ca/Si=1.00 (Fig. 4), which were used to derive K_{CSH}. The log $K_{CSH}=-7.07$ used by Borjesson et al. [31], taken directly from Greenberg and Chang [20], is not matched by the solubility data at Ca/Si=1.00 (Fig. 4) and may therefore be unreliable.

The values of log K_{CH} used by Kersten [30], Borjesson et al. [31] and Rahman et al. [32] (Table 2), were similarly in good agreement with the value reported here. However, log $K_{CH}=-5.435$ given in the LLNL database is notably different. This was determined from measured Gibbs free energy of formation values ([66] and references therein), which for CH was

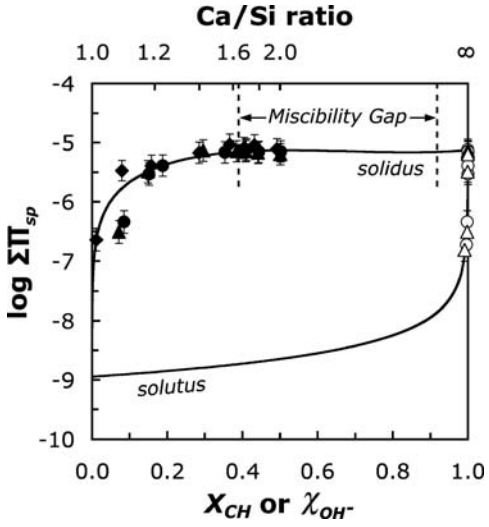

Fig. 5. Lippmann phase diagram representing the non-ideal CSH–CH SSAS. Solidus and solutus curves were drawn from Eqs. (2) and (5), respectively, where log $\sum \Pi_{sp}$ was plotted on the ordinate against two superimposed scales on the bottom abscissa: X_{CH} associated with the solidus curve (Ca/Si ratio from Eq. (1) is also shown on the top axis) and χ_{OH^-} associated with the solutus curve. Log K_{sp} values of the end-members components are log $K_{CSH}=-8.95$, S.D.=0.14, and log $K_{CH}=-5.13$, S.D.=0.04. The miscibility gap corresponds to $0.39<X_{CH}<0.92$ (equivalent to $1.64<Ca/Si<12.20$). Data points are plotted according to $\sum \Pi=\{Ca^{2+}\}(\{HSiO_3^-\}+\{OH^-\})\{OH^-\}$ on the solidus and equivalent values against χ_{OH^-} on the solutus: circles — week 64: triangles — week 80: diamonds — week 112. Error bars are the cumulative effect of pH±0.1, calcium ±2% and silicon ±5%.

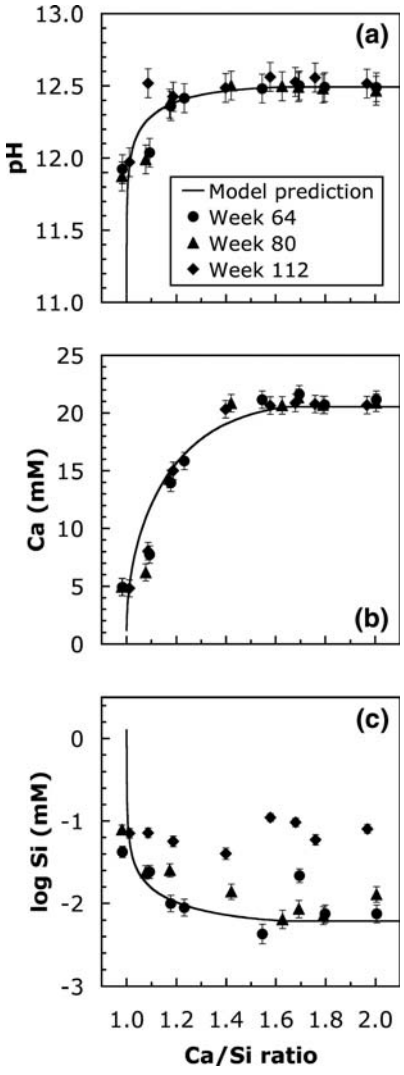

Fig. 6. CSH–CH SSAS model predictions (solid black line) plotted with the experimental solubility data (week 96 data omitted). (a) pH, error ±0.1: (b) Ca (mM), error ±2%: (c) log Si (mM), error ±5%.

−898408 J mol^{-1} ±1300. The error associated with this datum is significant because the calculated value of log $K_{CH}=-5.435\pm0.23$. Therefore, taking the upper and lower ranges of log K_{CH} values derived calorimetrically, log $K_{CH}=-5.205$ [66], and from the solubility data in this study, log $K_{CH}=-5.17$, respectively, are in better agreement. Other contributory factors to the discrepancy in log K_{CH} values would have been variations in the Gibbs free energy of formation of Ca^{2+} and OH^- ions, degree of carbonation, temperature, crystallinity, grain size, and equilibrium states of CH used in the experiments.

Although $X_{CH,1}=0.39$ was clearly defined by the occurrence of CH, the choice of $X_{CH,2}$ relied on fitting the solidus to the solubility data in the CSH–CH SSAS region ($Ca/Si<1.64$) using a least squares fitting algorithm. The best model fit used $X_{CH,2}=0.92$, $r^2=0.85$. This allowed the derivation of the Guggenheim parameters, α_0 and α_1 (Table 4), making it possible to solve Eqs. (2) and (5) and construct a Lippmann phase diagram (Fig. 5). The experimental data points closely

follow the calculated solidus and solutus curves supporting both the attainment of thermodynamic equilibrium after 64 weeks and the basis of using a non-ideal SSAS model to describe the dissolution of C–S–H gels at equilibrium for Ca/Si ≥ 1.0.

The solubility data points within the miscibility gap (Ca/Si > 1.64) also follow the predicted solidus, which was close to saturation with respect to the CH end-member for $X_{CH} > 0.39$ shown by the solidus being near horizontal for this compositional range; log $\sum \Pi_{sp} = -5.16$ at $X_{CH} = 0.39$ compared to log $\sum \Pi_{sp} = \log K_{CH} = -5.13$ at $X_{CH} = 1$. Satisfactory predictions can therefore be made within the miscibility gap, despite the corresponding solution being slightly undersaturated with respect to the CH end-member.

The composition of the aqueous phase, shown by the solutus, is skewed heavily in favor of the more soluble end-member, CH, and is characteristic of end-member K_{sp} values differing by more than three orders of magnitude [43,44]. This is consistent with the high pH and low silicon concentrations observed in the solubility data (Fig. 4). The incongruent dissolution behavior of C–S–H gels can therefore be accounted for using this modeling approach. However, the solutus also predicts the activity of $HSiO_3^-$, and therefore the concentration of silicon in solution, which only becomes significant when the composition of the C–S–H gel approaches CSH. Thus, using this modeling approach, the corresponding solution will be more undersaturated with respect to the CSH end-member than expected.

Encoding the values of K_{CSH}, K_{CH}, $X_{CH,1}$, and $X_{CH,2}$ (Table 4) into the SSAS feature of the computer program PHREEQC allowed the prediction of the more familiar pH, and calcium and silicon concentrations as a function of Ca/Si ratio in the solid phase(s) (Fig. 6). The model predicts the pH and calcium concentrations very well, not surprisingly since the more soluble CH has such a strong influence on the model prediction. As expected, the model predicts very low silicon concentrations because the solutus on the Lippmann phase diagram (Fig. 5), used to describe the solution composition, is heavily skewed towards the more soluble CH end-member. Despite this flaw, the model still provides a reasonable fit to the solubility data, is consistent and thermodynamically defensible, albeit semi-empirical, and can describe the incongruent dissolution of C–S–H gel for Ca/Si ≥ 1.00.

Because the model predicts very low silicon concentrations, the simulated dissolution of C–S–H gel would be suppressed more than it would in reality by the presence of this element in an invasive groundwater. Thus, the longevity of the C–S–H gel may be slightly overestimated according to this model.

Using a non-ideal CSH–CH SSAS is not without introducing its own set of limitations and should therefore be used with caution. Some of the key problems include that the model is currently only relevant at 25 °C, although the model would undoubtedly be flawed at higher temperatures with the expected precipitation of jennite [60]. Ionic strength corrections using the Davies equation are only accurate up to 0.3–0.5 molal. Kinetics and C–S–H gel interactions with other aqueous species are not accounted for, especially Mg^{2+}, Al^{3+}, CO_3^{2-}, SO_4^{2-}, and Cl^-, other than how their presence might influence pH. With further experiments to address some of these problems, better assessments will be made of the longevity of C–S–H gel and the pH buffer it can provide in the evolution of a nuclear waste repository.

Acknowledgements

This work was funded by a Natural Environment Research Council (NERC) CASE PhD studentship with contributions from Nirex, Nagra, and Castle Cement. We are indebted to Rory Wilson, Richard Brooker and Poon Cheung Choi who assisted us with the access and use of the PSD-XRD, FT-IR and ICP-AES instruments, respectively. We would also like to thank the anonymous reviewers whose suggestions improved this manuscript.

References

[1] D. Savage, The Scientific and Regulatory Basis for the Geological Disposal of Radioactive Waste, John Wiley & Sons Ltd, Chichester, 1995.
[2] M. Atkins, D. Damidot, F.P. Glasser, Performance of cementitious systems in the repository, Mater. Res. Soc. Symp. Proc. 333 (1994) 315–326.
[3] F.P. Glasser, M. Atkins, Cements in radioactive waste disposal, Mater. Res. Soc. Bull. (December 1994) 33–38.
[4] E.W. McDaniel, K.T. Othar, T.L. Sams, D.B. Delzer, W.D. Bostick, Basis for selecting cement-based waste forms for immobilizing radioactive waste, Mater. Res. Soc. Symp. Proc. 127 (1989) 421–430.
[5] M. Atkins, F.P. Glasser, A. Kindness, D.E. Macphee, Solubility data for cement hydrate phases (25 °C), DoE(UK), DoE/HMIP/PR/91/032, 1991.
[6] A. Haworth, S.M. Sharland, C.J. Tweed, Modelling of the degradation of cement in a nuclear waste repository, Mater. Res. Soc. Symp. Proc. 127 (1989) 447–454.
[7] A. Atkinson, D.J. Goult, J.A. Hearne, An assessment of the long term durability of concrete in radioactive waste repositories, Mater. Res. Soc. Symp. Proc. 50 (1985) 239–246.
[8] A. Atkinson, N.M. Everitt, R.M. Guppy, Time dependence of pH in a cementitious repository, Mater. Res. Soc. Symp. Proc. 127 (1989) 439–446.
[9] F.P. Glasser, Progress in the immobilization of radioactive wastes in cement, Cem. Concr. Res. 22 (1992) 201–216.
[10] U. Berner, Evolution of pore water chemistry during degradation of cement in a radioactive waste repository environment, Waste Manage. 12 (1992) 201–219.
[11] S. Goto, M. Daimon, G. Hosaka, R. Kondo, Composition and morphology of hydrated tricalcium silicate, J. Am. Ceram. Soc. 59 (7–8) (1976) 281–284.
[12] X. Zhang, W. Chang, T. Zhang, C.K. Ong, Nanostructure of calcium silicate hydrate gels in cement paste, J. Am. Ceram. Soc. 83 (10) (2000) 2600–2604.
[13] D. Viehland, J.F. Li, L.J. Yuan, Z.K. Xu, Mesostructure of calcium silicate hydrate (C–S–H) gels in portland cement paste: short-range ordering, nanocrystallinity, and local compositional order, J. Am. Ceram. Soc. 79 (7) (1996) 1731–1744.
[14] D. Viehland, Z. Xu, Observation of a mesostructure in calcium silicate hydrate gels of portland cement, Phys. Rev. Lett. 77 (5) (1996) 952–955.
[15] H.F.W. Taylor, Cement Chemistry, Academic Press, London, 1997.
[16] E.P. Flint, L.S. Wells, Study of the system CaO–SiO2–H2O at 30 °C and of the reaction of water on anhydrous calcium silicates, J. Res. Natl. Bur. Stand. 12 (1934) 751–783.
[17] P.S. Roller, G. Ervin Jr., The system calcium–silica–water at 30°. The association of silicate ion in dilute alkaline solution, J. Am. Chem. Soc. 62 (3) (1940) 461–471.
[18] H.F.W. Taylor, Hydrated calcium silicates. Part I. Compound formation at ordinary temperature, J. Chem. Soc. 726 (1950) 3682–3690.
[19] G. Kalousek, Application of differential thermal analysis in a study of the system lime–silica–water, Third International Symposium on the Chemistry of Cement, Cement and Concrete Association, London, 1952.

[20] S.A. Greenberg, T.N. Chang, Investigation of the colloidal hydrated calcium silicates. II. Solubility relationships in the calcium–silica–water system at 25 °C, J. Phys. Chem. 69 (1965) 182–188.
[21] K. Fujii, W. Kondo, Heterogeneous equilibrium of calcium silicate hydrate in water at 30 °C, J. Chem. Soc. Dalton Trans. 2 (1981) 645–651.
[22] A. Atkinson, D.J. Goult, C.F. Knights, Aqueous chemistry and thermodynamic modelling of $CaO–SiO_2–H_2O$ gels, DoE(UK), DOE/RW/87.048, 1987.
[23] X. Cong, R.J. Kirkpatrick, ^{29}Si MAS NMR of the structure of calcium silicate hydrate, Adv. Cem. Based Mater. 3 (1996) 144–156.
[24] J.J. Chen, J.J. Thomas, H.F.W. Taylor, H.M. Jennings, Solubility and structure of calcium silicate hydrate, Cem. Concr. Res. 34 (2004) 1499–1519.
[25] F.P. Glasser, D.E. MacPhee, E.E. Lachowski, Solubility modelling of cements: implications for radioactive waste immobilisation, Mater. Res. Soc. Symp. Proc. 84 (1987) 331–341.
[26] U.R. Berner, Modelling the incongruent dissolution of hydrated cement minerals, Radiochim. Acta 44/45 (1988) 387–393.
[27] V.A. Sinitsyn, D.A. Kulik, M.S. Khodorivsky, I.K. Kaprov, Prediction of solid–aqueous equilibria in cementitious systems using Gibbs energy minimization: I. Multiphase aqueous–ideal solid solution models, Mater. Res. Soc. Symp. Proc. 506 (1998) 953–960.
[28] D.A. Kulik, V.A. Sinitsyn, I.K. Kaprov, Prediction of solid–aqueous equilibria in cementitious system using Gibbs energy minimization: II. Dual thermodynamic approach to estimation of the non-ideality and end-member parameters, Mater. Res. Soc. Symp. Proc. 506 (1998) 983–990.
[29] D.A. Kulik, M. Kersten, Aqueous solubility diagrams for cementitious waste stabilization systems: II, end-member stoichiometries of ideal calcium silicate hydrate solid solutions, J. Am. Ceram. Soc. 84 (12) (2001) 3017–3026.
[30] M. Kersten, Aqueous solubility diagrams for cementitious waste stabilization systems. 1. The C–S–H solid–solution system, Environ. Sci. Technol. 30 (7) (1996) 2286–2293.
[31] S. Börjesson, A. Emrén, C. Ekberg, Thermodynamic model for the calcium silicate hydrate gel, modelled as a non-ideal binary solid solution, Cem. Concr. Res. 27 (11) (1997) 1649–1657.
[32] M.M. Rahman, S. Nagasaki, S. Tanaka, A model for dissolution of $CaO–SiO_2–H_2O$ gel at $Ca/Si>1$, Cem. Concr. Res. 29 (1999) 1091–1097.
[33] H.F.W. Taylor, Tobermorite, jennite, and cement gel, Z. Kristallogr. 202 (1/2) (1992) 41–50.
[34] D.A. Kulik, S.A. Dmitriev, K.V. Chudnenko, I.K. Kaprov, V.A. Sinitsyn, S.U. Aja, et al., Selektor-A version 3.1.289-beta. Integrated program and database to calculate geochemical equilibria by Gibbs energy minimization (English version), Brooklyn-Kiev, 1997, p. 270.
[35] D.A. Kulik, U. Berner, E. Curti, Modelling chemical equilibrium partitioning with the GEMS-PSI code, in: B. Smith, B. Gschwend (Eds.), PSI Scientific, Report 2003/ Volume IV, Paul Scherrer Institute, Villegen, Switzerland, 2004, pp. 109–122.
[36] D. Read, W.S. Atkins, CHEMVAL 6, Thermodynamic database, London, 1995.
[37] H. Stade, W. Wieker, Structure of ill-crystallised calcium silicate hydrate silicates, Z. Anorg. Allg. Chem. 466 (1980) 55–70.
[38] M. Grutzeck, A. Benesi, B. Fanning, Silicon-29 magic angle spinning nuclear magnetic resonance study of calcium silicate hydrates, J. Am. Ceram. Soc. 72 (1989) 665–668.
[39] P.D. Glynn, MBSSAS: a code for the computation of Margules parameters and equilibrium relations in the binary solid-solution aqueous-solution systems, Comput. Geosci. 17 (1991) 907–966.
[40] F. Lippmann, The solubility product of complex minerals, mixed crystals and three-layer clay minerals, Neues Jahrb. Mineral. Abh. 130 (1977) 243–263.
[41] F. Lippmann, Stable and metastable solubility diagrams for the system $CaCO_3–MgCO_3–H_2O$ at ordinary temperature, Bull. Mineral. 105 (1982) 273–279.
[42] F. Lippmann, Phase diagrams depicting aqueous solubility of binary mineral systems, Neues Jahrb. Mineral. Abh. 139 (1) (1980) 1–25.
[43] P. Glynn, Modeling solid-solution reactions in low-temperature aqueous systems, in: D.C. Melchior, R.L. Bassett (Eds.), Chemical Modeling of Aqueous Systems, vol. II, American Chemical Society, Washington, D.C., 1990, pp. 74–86.
[44] P.D. Glynn, E.J. Reardon, L.N. Plummer, E. Busenberg, Reaction paths and equilibrium end-points in solid-solution aqueous-solution systems, Geochim. Cosmochim. Acta 54 (1990) 267–282.
[45] P.D. Glynn, E.J. Reardon, Solid-solution aqueous solution equilibria: thermodynamic theory and representation, Am. J. Sci. 290 (1990) 164–201.
[46] D.L. Parkhurst, C.A.J. Appelo, PHREEQC 2: A Computer Program for Speciation, Batch-Reaction, One-Dimensional Transport and Inverse Geochemical Calculations, USGS, Denver, 2001.
[47] E.A. Guggenheim, Theoretical basis of Raoult's law, Trans. Faraday Soc. 33 (1) (1937) 151–159.
[48] E.A. Guggenheim, Mixtures: The Theory of the Equilibrium Properties of Some Simple Classes of Mixtures, Solutions and Alloys, Oxford University Press, London, 1952.
[49] P.D. Glynn, D.L. Parkhurst, Modeling non-ideal solid-solution aqueous-solution reactions in mass-transfer computer codes, Water–Rock Interaction, Proceedings of the Seventh International Symposium on Water Rock Interactions, A.A. Balkema, Rotterdam, 1992.
[50] M. Thompson, J.N. Walsh, Handbook of Inductively Coupled Plasma Spectrometry, Blackie, Glasgow, 1983.
[51] E.J. Conway, Microdiffusion Analysis and Volumetric Error, Crosby Lockwood and Sons, London, 1962.
[52] J. Ballon, V. Comparat, J. Pouxe, The blade chamber: the solution for curved gaseous detectors, Nucl. Instrum. Methods 217 (1983) 213–216.
[53] M. Evain, P. Deniard, A. Jouanneaux, R. Brec, Potential of the INEL X-ray position-sensitive detector: a general study of the Debye–Scherrer setting, J. Appl. Crystallogr. 26 (1993) 563–569.
[54] C.W. Davies, Ion Association, Butterworths, Washington, D.C., 1962.
[55] I. Klur, B. Pollet, J. Virlet, A. Nonat, C–S–H structure evolution with calcium content by multinuclear NMR, in: P. Colombet (Ed.), NMR Spectroscopy of Cement Based Materials, Springer-Verlag, Berlin, 1997, pp. 119–142.
[56] J.D.C. McConnell, The hydrated calcium silicates riversideite, tobermorite, and plombierite, Mineral. Mag. 30 (1954) 293–305.
[57] J.A. Gard, H.F.W. Taylor, Calcium silicate hydrate (II) ("C–S–H(II)"), Cem. Concr. Res. 6 (1976) 667–678.
[58] E. Bonaccorsi, S. Merlino, H.F.W. Taylor, The crystal structure of jennite, $Ca_9Si_6O_{18}(OH)_6{:}8H_2O$, Cem. Concr. Res. 34 (9) (2004) 1481–1488.
[59] A.B. Carpenter, R.A. Chalmers, J.A. Gard, K. Speakman, H.F.W. Taylor, Jennite, a new mineral, Am. Mineral. 51 (1966) 56–74.
[60] N. Hara, N. Inoue, Formation of jennite from fumed silica, Cem. Concr. Res. 10 (1980) 677–682.
[61] E. Bonaccorsi, S. Merlino, A.R. Kampf, The crystal structure of tobermorite 14 Å (plombierite), a C–S–H phase, J. Am. Ceram. Soc. 88 (3) (2005) 505–512.
[62] H. Noma, Y. Adachi, H. Yamada, T. Nishino, ^{29}Si MAS NMR spectroscopy of poorly-crystalline calcium silicate hydrates (C–S–H), in: P. Colombet (Ed.), NMR Spectroscopy of Cement Based Materials, Springer-Verlag, Berlin, 1997, pp. 159–168.
[63] X. Cong, R.J. Kirkpatrick, ^{29}Si and ^{17}O NMR investigation of the structure of some crystalline calcium silicate hydrates, Adv. Cem. Based Mater. 3 (1996) 133–143.
[64] H.F.W. Taylor, A disucssion of the papers "Models for the composition and structure of calcium silicate hydrate (C–S–H) gel in hardened tricalcium silicate pastes" and "The incorporation of minor and trace elements into calcium silicate hydrate (C–S–H) gel in hardened cement pastes" by I. G. Richardson and G. W. Groves, Cem. Concr. Res. 23 (1993) 995–998.
[65] I.G. Richardson, G.W. Groves, Models for the composition and structure of calcium silicate hydrate (C–S–H) gel in hardened tricalcium silicate pastes, Cem. Concr. Res. 22 (6) (1992) 1001–1010.
[66] R.A. Robie, B.S. Hemingway, J.R. Fisher, Thermodynamic properties of minerals and related substances at 298.15 K and 1 bar (10^5 Pa) pressure and at higher temperatures, U.S. Geol. Surv. Bull. 1452 (1979) 456.